The irreversible thermal expansion of an energetic material

Hervé Trumel[1], François Willot[2], Thomas Peyres[1], Maxime Biessy[1], and François Rabette[1,2]

[1] CEA, DAM, Le Ripault, F-37260 Monts, France
[2] Mines ParisTech, PSL - Research University, Centre for Mathematical Morphology, F-77300 Fontainebleau, France

The works deals with a macroscopically isotropic energetic material based on triamino-trinitrobenzene crystals bonded with a small volume fraction of a thermoplastic polymer. This material is shown experimentally to display an irreversible thermal expansion behavior characterized by dilatancy and variations of its thermal expansion coefficient when heated or cooled outside a narrow reversibility temperature range. The analysis of cooling results suggests the existence of residual stresses in the initial state, attributed to the manufacturing process. Microstructure-level FFT computations including the very strong anisotropic thermoelastic triamino-trinitrobenzene crystal response and temperature-dependent binder plasticity, show that strong internal stresses develop in the disoriented crystals under thermal loading, either heating or cooling. Upon cooling, binder plastic yielding is hindered, thus promoting essentially brittle microcracking, while it is favoured upon heating. Despite its low volume fraction, the role of the binder is essential, its plastic yielding causing stress redistribution and residual stresses upon cooling back to ambient.

Keywords: jointed polycrystal, thermal expansion, thermoelastic anisotropy, microcracking, FFT-based homogenization, internal stresses, polymer plasticity, glass transition

1 Introduction

Many energetic materials, i.e. solid explosives and propellants, are particulate composites made of explosive (or fuel-oxidizer mixture) grains bound together with an inert polymer. As their main purpose is to deliver as large quantities of hot gases as possible, the amount of binder is kept to a minimum without jeopardizing their safety properties. As a result, solid propellants incorporate at least 15 % (vol.) elastomeric binder, whereas some plastic-bonded explosives may contain binder volume fractions as low as 5 %, and even below.

So-called composite solid propellants and alike explosives are most often manufactured by dispersing the filler into the liquid binder containing a crosslinking agent, vacuum-casting the mixture and curing at moderate temperature, resulting in highly-filled elastomeric materials. In this case, the high packing density can only be reached by optimizing the grain size distribution of the filler, and microstructures are often found, in which large grains are embedded in a composite matrix composed of the smallest grains and binder. However, the mixture must be castable, which is no longer possible for very low binder volume fractions. In this case, a slurry process is used to coat the filler with the binder, and the dried coated powder is pressed at relatively high pressure and moderate temperature.

The quasi-static thermomechanical behavior of both classes of energetic materials displays common features, although their ductility is obviously reduced when the binder fraction decreases. At low stress triaxiality, such as uniaxial tension or compression, they undergo damage and strain softening (see Xu et al. (2008); Ellis et al. (2005); Le et al. (2010), for instance), mainly by filler-binder debonding (Rae et al. 2002), possibly by filler fracture (Williamson et al. 2007; Trumel et al. 2010), until ultimate fracture at 10-150 % strain for solid propellants, 1-5 % strain for

pressed explosives. At high stress triaxiality, such as triaxial compression, damage is partially inhibited, filler plasticity may be promoted, and ductility increases strongly with confining pressure (Trumel et al. 2010; Wiegand et al. 2011). Additionally, binder-induced viscoelasticity is always displayed, even for very low binder fractions (Drodge et al. 2010; Picart and Brigolle 2010).

Therefore, polymer-bonded energetic materials exhibit a continuum of thermomechanical behaviors when the binder fraction decreases, provided that the binder phase remains continuous, while direct grain-grain contact force chains must be considered if the binder phase is not continuous (Bennett and Luscher 2019). Within this class of energetic materials, however, pressed explosives based on 1,3,5-triamino-2,4,6-trinitrobenzene (TATB) display an additional peculiarity, namely irreversible thermal expansion. Under repeated thermal cycling, a progressive and irreversible increase of the specific volume, i.e. dilatancy, is observed, and tends, for a large number of cycles, to an asymptotic value dependent on the minimum/maximum temperature of the thermal cycles (see Thompson et al. (2019) for a recent overview). This phenomenon is generally referred to as "ratchet growth".

Kolb and Rizzo (1979) were the first to investigate ratchet growth, and showed that thermal expansion of the TATB crystal is totally reversible, slightly nonlinear, and strongly anisotropic. The TATB molecule is almost planar, and assembles in hexagonal graphitic planes through strong hydrogen bonds between nitro- and amino- groups, whereas graphitic planes stack together in a triclinic unit cell via weak van der Waals bonding (Cady and Larson 1965), thus explaining the strongly anisotropic thermoelastic behavior of the TATB crystal. Kolb and Rizzo (1979) suggested that thermal expansion anisotropy be responsible for dilatancy, due to thermal expansion incompatibilities of randomly oriented crystals within the explosive aggregate. Rizzo et al. (1981) showed that the magnitude of ratchet growth is highest in binder-free pressed TATB, and that the magnitude of dilatancy is strongly dependent on the binder.

Maienschein and Garcia (2002) performed thermal expansion experiments at high temperature on die-pressed LX-17, a TATB-based explosive with 7.5 % (mass) of a semi-crystalline binder with a close to ambient glass transition temperature of 28 °C. They first observed macroscopic thermal expansion anisotropy, which is nowadays known as the consequence of strong texture induced by die-pressing (Skidmore et al. 2003; Thompson et al. 2010; Schwarz et al. 2013; Schwarz et al. 2005). Then, they studied the influence of pressing temperature on ratchet growth, and showed that dilatancy increases when temperature is held constant during several hours. Woznick et al. (2018) and Thompson et al. (2019) performed thermal expansion experiments on binder-free pressed TATB and PBX 9502, an explosive very similar to LX-17, with only 5 % of the same binder. They showed that binder-free TATB displays the largest dilatancy, and that both materials, submitted to alternate hot and cold thermal cycles, display enhanced dilatancy. Additionally, the authors showed that low temperature thermal cycles indeed induce dilatancy, although much less than at high temperature. Willey et al. (2006) and Willey et al. (2009) investigated the change in porosity between pristine and thermally cycled LX-17 and other TATB-based explosives by ultra-small angle X-ray scattering, and showed an increase of the number and size of large (i.e. micron-sized) pores. Armstrong and Mang (2021) performed a similar study by small-angle neutron scattering on PBX 9502, and showed that micron-sized pores grow until 120 °C, and that new pores appear above this temperature. They found, additionally, some residual growth after cooling back to ambient.

Gee et al. (2007) and later Willey et al. (2009) performed mesoscale computations, using a coarse numerical method derived from molecular dynamics, including a binder-filler adhesion model. They found that new pores only appear after crossing the glass transition, and that they are strongly correlated with grain relative motions, thereby confirming the proposition of Kolb and Rizzo (1979). They showed that binders with high glass transition temperatures can efficiently hinder ratchet growth, but with the proviso that their adhesive strength is high. Additionally, they pointed at the adhesive strength of [001] facets of TATB grains as the weakest link of the systems.

Ambos et al. (2015) and Gasnier et al. (2018a); Gasnier et al. (2018b) investigated a TATB-based explosive using an amorphous binder with a glass transition temperature of ~100 °C (see Section 2). They performed an exploratory experimental study of the thermal expansion of this material, and found classical ratchet growth for thermal cycles above the glass transition of

the binder. Investigating temperature cycling below ambient, they showed that irreversible thermal expansion is accompanied with a strong decrease of the volumetric thermal expansion coefficient, as low as 40 % for cycles at −100 °C, with quite small levels of dilatancy. They used a Fourier-based (FFT) full-field homogenization method, on virtual microstructures mimicking that of the actual explosive but neglecting the binder, assuming random TATB crystal orientations and perfect grain-grain bonding to interpret experimental findings. Using TATB single crystal anisotropic elastic coefficients from Bedrov et al. (2009) and thermal expansion ones from Sun et al. (2010), they found that the ambient temperature effective coefficient of volumetric thermal expansion is predicted to ∼2 % accuracy, and that strong internal stresses are induced by thermal loading. Then, they performed additional calculations of microstructures containing variable densities of inter- or transgranular microcracks, with but little effect of the effective thermal expansion coefficient. The only way to induce a decrease of this coefficient is to correlate the microcrack orientations to those of the TATB crystals, and more precisely when microcrak normals are orthogonal to the graphitic plane of TATB crystal, thereby confirming the concept of [001] TATB crystal facets as weakest links put forward by Gee et al. (2007).

The purpose of the present paper is to complement the experimental investigations of Gasnier et al. (2018b) for a better understanding of the thermal expansion of the same explosive material. The focus will be put first on low temperature experiments, then on alternate thermal cycling. The paper is organized as follows. Section 2 presents the material and its microstructure. Experiments are described and discussed in Section 3, while Section 4 is devoted to mesoscale FFT computations, the emphasis being put on the role of binder plasticity. Experimental and numerical results are commented in Section 5, and a brief summary and plans for future work are proposed in Section 6.

2   The material

The material of interest, referred to as "the composite" in the sequel, is a macroscopically isotropic TATB-based explosive, isostatically pressed with ∼4.5 % (vol.) of an amorphous polymeric binder (glass transition temperature ca. 100 °C) to less than 3 % porosity, easy to machine and to polish. As illustrated in Figure 1, it appears under polarized light microscopy as a polycrystalline aggregate of TATB grains. Most grain boundaries are not clearly delineated, and the binder is not
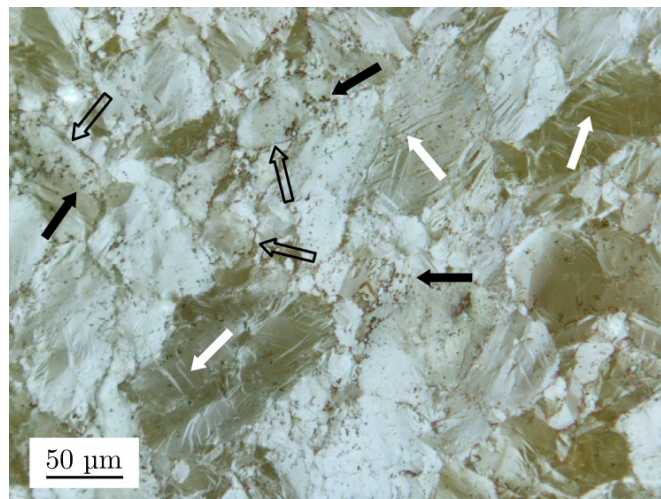

Figure 1   Microstructure of the composite (polarized reflected light microscopy). Black arrows: pores and pore clusters. White arrows: probable deformation twins. Open arrows: possible intra-transgranular microcracks.

visible, suggesting that it be present in the form of thin layers. At this scale, some defects are clearly seen, such as pores and pore clusters (black arrows) and bands (white arrows). Being absent from the initial TATB powder, the latter are induced by the pressing process, and are thought to result from the twinning process recently described by Lafourcade et al. (2018) and Lafourcade et al. (2019).

Its thermomechanical behavior was described in Gasnier et al. (2018b), and will only be outlined in the following. It is quasi-brittle at low triaxiality loading, with failure at ∼1.5 %

longitudinal strain under uniaxial quasi-static compression, and quite ductile under triaxial compression at 200 MPa confining pressure, for which failure is not observed, even at 40 % strain. The ambient temperature bulk and shear elastic moduli are 7.2 and 2.7 GPa respectively, whereas the volumetric coefficient of thermal expansion is $1.45 \times 10^{-4}\,K^{-1}$. As already mentioned in the Introduction, Gasnier et al. (2018b) were able to retrieve the latter numerically to an excellent accuracy, but not the former, and proposed that the material, in its initial state, contains a population of randomly distributed intergranular microcracks. In Figure 1, the open arrows point at such possible defects, although the only way to identify them with confidence would be to perform observations under (low stress) tensile loading, in order to open present cracks and make them more visible. Such experiments are planned, but have not been performed at present.

3   Experimental

3.1   Method

The cyclic thermal expansion experiments presented below were performed on a Netzsch DIL 402 SE double stage horizontal dilatometer. Each experiment involved a 5 mm $\times$ 5 mm $\times$ 50 mm explosive sample and a reference polycrystalline aluminum one of the same geometry, with an applied force of 0.1 N. In order to minimize temperature gradients, the heating/cooling rate was $10\,°C\,h^{-1}$ ($0.16\,°C\,min^{-1}$), and each thermal cycle involved a time lag of 30 min at maximum or minimum temperature. Temperature equilibration was favoured by a helium flow of $10\,ml\,min^{-1}$ in the chamber of the dilatometer. These experimental conditions hold for all experiments, except otherwise mentioned.

The thermal control accuracy is better than $0.1\,°C$, and the end of each heating or cooling phase involves an slight overshoot of around $0.1\,°C$, needing about one minute to reach prescribed temperature. The resolution of displacement measurements is $0.5\,\mu m$. All results will be given as thermal strains, defined by the ratio of measured displacements to initial sample length, with a relative uncertainty of the order of 0.2 %, and as thermal expansion coefficients, defined by the slope of strain-temperature curves, with an uncertainty or the order of 0.4 %. As will be seen below, the standard deviation of the volumetric thermal expansion coefficient in the initial state is 4 % on 16 experiments. It was observed (not shown) that the strain-temperature curves obtained on different samples for a given thermal load coincide with each other within 1.2 % of the measured strain at most (notice that all samples were machined from the same batch). However, only the shortest experiments (single heating-cooling cycles) were repeated.

Since temperature variations imply Young's modulus ones, it was judged that a dedicated experiment was necessary to assess the influence of the applied force on thermal strain measurements. It was performed in the range 20-140 °C, the maximum temperature involved in this study, at which the Young's modulus should be minimum. For this experiment, heating was performed at a 0.01 N force, whereas a force jump from 0.01 N to 0.1 N was applied at the beginning of the 30 min time lags every 10 °C from 80 to 140 °C. The strain jump magnitudes were of the order of 5×10^{-5}, did not vary appreciably for all temperatures, and were quite similar for the aluminum reference sample. Therefore, these strain jumps can be attributed to the low stiffness of the displacement measurement system, that does not vary appreciably with temperature. Hence, the strain measurement bias can be considered negligible, provided that the applied force does not vary during the whole experiment. For illustrative purposes, a jump from 0.01 to 1 N was also performed at 140 °C, and resulted in a strain jump of 2.1×10^{-4}, which would not be acceptable in the present context.

3.2   First findings

To begin with, Figure 2 shows the results of two cyclic experiments, one above (in red) and one below (in blue) room temperature. On the high temperature side, linearity is lost around 75 °C, and the slope of the thermogram increases dramatically, and triples at 140 °C, going from $5.01 \times 10^{-5}\,K^{-1}$ at room temperature to $1.51 \times 10^{-4}\,K^{-1}$. Irreversibility is clear from the cooling curve, whose slope at 140 °C is $1.01 \times 10^{-4}\,K^{-1}$, and decreases smoothly with temperature. The residual strain at room temperature is 0.18 %.

Figure 2   Two cyclic experiments below (blue) and above (red) room temperature.
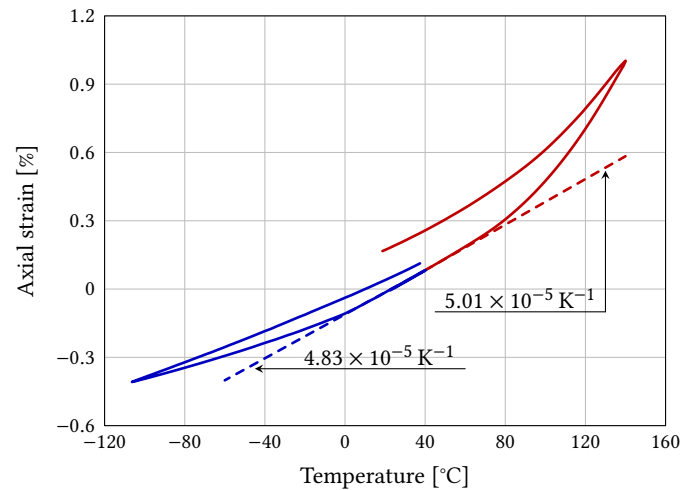

On the low temperature side, the slope of the linear part of the thermogram is $4.83 \times 10^{-5}\,\mathrm{K}^{-1}$. Linearity is lost at around $5\,°\mathrm{C}$, and irreversibility is again clearly evidenced by the re-heating curve, strictly linear up to $-50\,°\mathrm{C}$, with a slope of $3.29 \times 10^{-5}\,\mathrm{K}^{-1}$. This slope increases smoothly with temperature, and the residual strain at room temperature is $0.04\,\%$.

Summarizing, both high and low temperature cycles are irreversible, and both induce dilatancy, although of a lower magnitude at low temperature, and the slope of the thermograms varies strongly with temperature. Both display a (rather limited) linear range, associated with virtually identical ($4\,\%$ difference) slopes. The phenomenologies of the high and low temperature thermograms appear somewhat different, but more details are required to be more precise.

3.3   Investigations above ambient temperature

A first experiment, already reported in Gasnier et al. (2018b), is designed to find the linearity limit and to study cooling. For this purpose, a series of cycles are performed from ambient temperature to maximum temperatures of 40, 60, 70, 80 and $90\,°\mathrm{C}$, just below the glass transition temperature, and to a final cooling-heating cycle to $-30\,°\mathrm{C}$, the result being displayed in Figure 3. Some accidents can be observed on the thermogram. These artifacts are due to a malfunction of

Figure 3   Cycles from ambient temperature to maximum temperatures of 40, 60, 70, 80, 90 and $-30\,°\mathrm{C}$. The cycles to 40, 60 and $70\,°\mathrm{C}$ are reversible. Inset: enlargement near ambient temperature. The dashed lines are the linear approximations of the last two cooling phases and the arrow marks the point from which the last cooling departs from linearity, indicating the beginning of irreversible behavior.
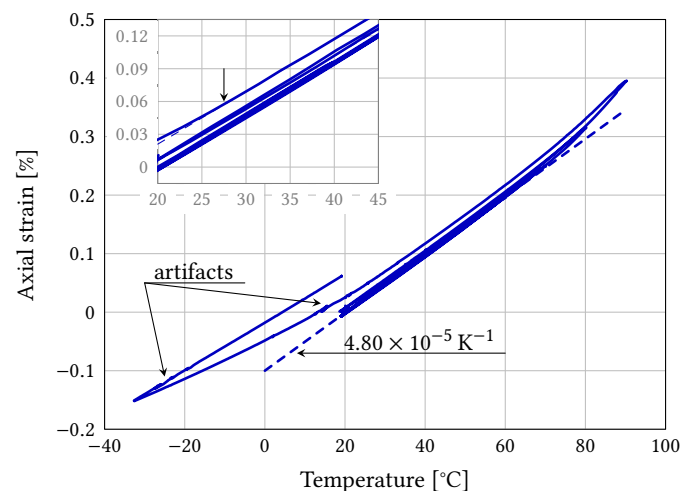

the cold nitrogen supply. The cycles at 40, 60 and $70\,°\mathrm{C}$ are strictly reversible. The first two are linear, whereas the latter is slightly nonlinear. Their common slope is $4.91 \times 10^{-5}\,\mathrm{K}^{-1}$ at room temperature.

The cycle at $80\,°\mathrm{C}$ induces a slight dilatancy of $0.025\,\%$ and the slope after cooling does not change. Therefore, the reversibility limit for the material in its initial state lies between 70 and $80\,°\mathrm{C}$, say $75\,°\mathrm{C}$. For the cycle at $90\,°\mathrm{C}$, the dilatancy is $0.056\,\%$ and, again, the slope remains unchanged, at least down to $30\,°\mathrm{C}$. Below this limit, the slope increases slightly. It is also observed that each cooling coincides with the subsequent re-heating to a very good approximation.

A similar experiment is then performed at higher temperatures. In order to estimate the slope of linear part of the thermograms, if any, the lowest temperature of the cycles is set to 50 °C. Therefore, a series of cycles are performed from 50 °C to maximum temperatures of 90, 100, 110, 120, 130 and 140 °C, well above the glass transition temperature for the last four cycles, and to a final cooling-heating cycle to −30 °C, the result being displayed in Figure 4.

Figure 4   Cycles from 50 °C to maximum temperatures of 90, 100, 110, 120, 130, 140 and −30 °C.
Inset: enlargement to show the details in the glassy domain and just above.
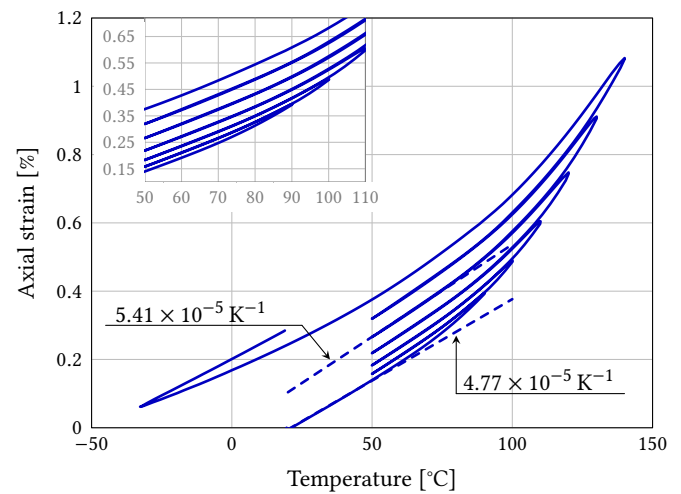
The residual strain increment observed at 50 °C at the end of each cycle increases with maximum temperature, except for the cycle at 140 °C. All cooling phases end up with a linear part, the slope of which increases with maximum temperature (see Figure 4), again, except the cycle at 140 °C. As before, the re-heating curves coincide with the cooling one of the preceding cycle, thus indicating reversibility, except in a small range near the maximum temperature of each cycle. This suggests a small time dependence upon heating. The residual strain at room temperature is 0.24 %, to be compared with the 0.18 % measured at the end of the single cycle to 140 °C of Figure 2. Finally, the absence of a linear phase upon cooling from 140 to 50 °C suggests that cooling is irreversible at 50 °C.

In order to examine the question of time dependence, the experiment dedicated to the influence of force also comprised 6 h temperature creep at a 0.1 N force followed by another 6 h at 0.01 N, at temperatures of 90, 100, 110, 120, 130, 140 and 130 °C. This experiment (see Figure 5) shows that a small but measurable creep takes place during the plateaus. Its magnitude,

Figure 5   Thermal creep experiment (blue) performed at 80, 90, 100, 110, 120, 130, 140 and 130 °C versus single cycle to 140 °C (red).
Inset: force vs. time.
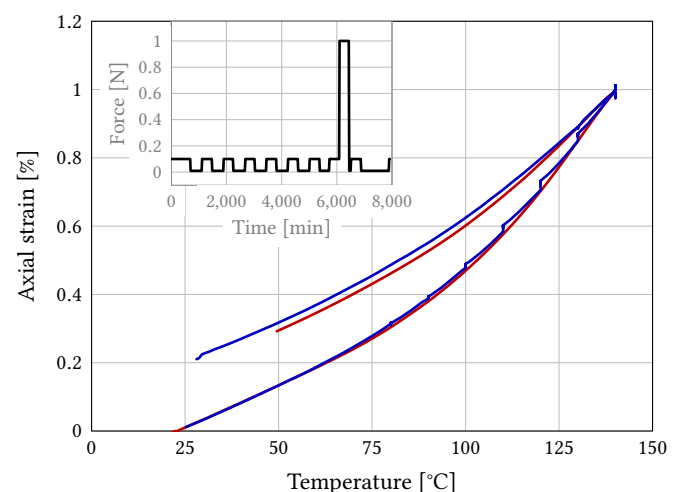
negligible at 80 °C, is highest, of the order of 0.02 %, at 110-130 °C. After 12 h, thermal creep is not quite complete, but equilibrium is almost reached.

The comparison with the high temperature cycle of Figure 2 shows a significant difference between relaxed points, at the end of each creep phase, and monotonous heating (or cooling). The difference is maximum at 110-120 °C, and tends to wear off at higher temperature. It is also seen that creep is much less pronounced upon cooling, which can probably be considered in

quasi-equilibrium, at least down to the glass transition.

3.4 Investigations below ambient temperature

The results of two cyclic experiments are displayed in Figure 6. The first one (dark blue) is

Figure 6 Two experiments with cycles from 50 °C to minimum temperatures of 0 °C, −25 °C, −50 °C (dark blue), and −75 °C, −100 °C, −130 °C (light blue).
Inset: magnification around room temperature showing the hysteresis loops upon heating and re-cooling for the −130 °C experiment.
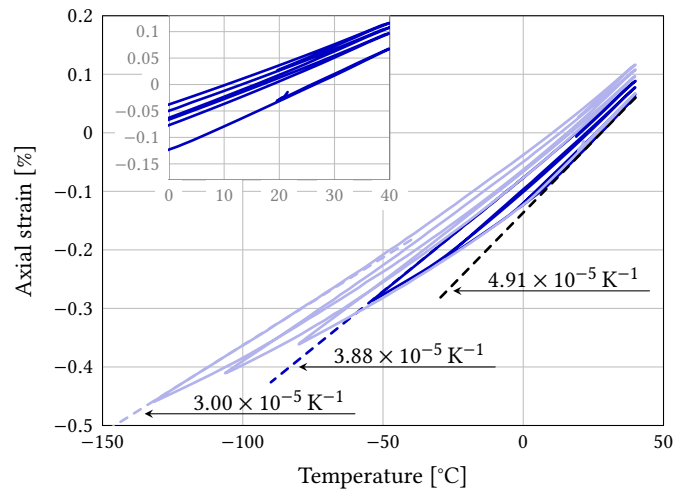

performed from 40 to 0, −25 and −50 °C, and the second one (light blue) from 40 to −75, −100 and −130 °C. Both experiments start with a linear phase, the slope of which is identical at $4.91 \times 10^{-5} \, \text{K}^{-1}$. Linearity is lost at ~5 °C. Each re-heating phase begins with a linear segment, whose slope decreases monotonically with the minimum temperature reached previously (see Figure 6). Upon heating, linearity is eventually lost, and the slope increases smoothly to reach the initial value, except for the cycle at the lowest temperature. The lowest slope is $3.0 \times 10^{-5} \, \text{K}^{-1}$, which represents a 40 % decrease from to its initial value. The residual strains at room temperature are 0.033 and 0.055 % for the experiments at −50 and −130 °C, respectively.

For each experiment, the minimum temperature loci of each cycle forms an envelope that coincides with monotonous experiments (not shown). The two experiments shown in Figure 6 do not match exactly, which is attributed to the variability of the composite. They are nevertheless close, and will be analyzed as a single curve in what follows.

Noticing that all linear parts of re-heating phases seem to converge towards a unique origin, Gasnier et al. (2018b) sought its coordinates and the slopes of linear parts of each re-heating phases by optimization to match experimental data in a least square sense. The optimization process was successful and described correctly the data, as shown in Figure 7, except perhaps for the cycle at the lowest temperature, and a common origin was found at 45.7 °C, with a corresponding strain of 0.091 %.

Figure 7 Common origin of the linear parts of each re-heating phases, found by optimization.
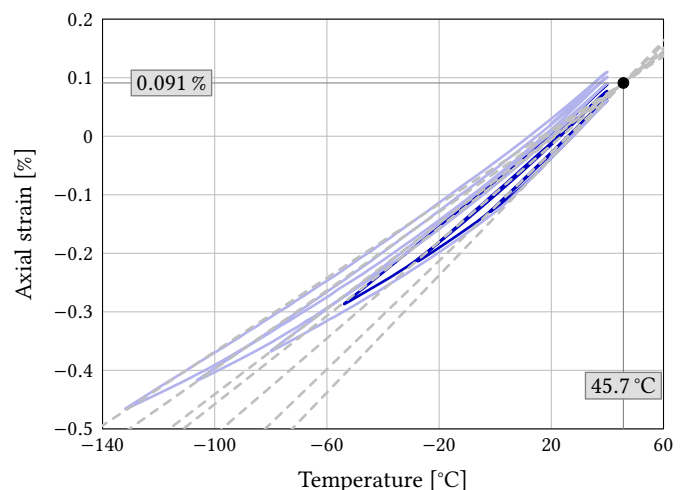

The common origin is of course an approximation. For example, a closer look to Figure 7 shows that re-heating from the lowest temperature could be better restituted. However, if this

cycle is omitted in the optimization process, the common origin changes by no more than 1 °C and 0.01 % strain. Therefore, this approximation seems rather robust.

3.5   Effect of pre-heating

Up to now, only hot or cold thermal cycles have been investigated. Let us now examine some more complex cases. Two experiments are first performed, in which cold cycles are preceded by a high temperature excursion, at 90 °C for the first experiment, at 140 °C for the second one. The result is displayed in Figure 8 and compared with those of Figure 6. The effect of pre-heating at

Figure 8   Cold cycles after an excursion at 90 °C (green) and at 140 °C (red), compared to the data of Figure 6 (light blue). The open circles indicate the common origin of each experiment. Dashed curves: see text and Equation (1).
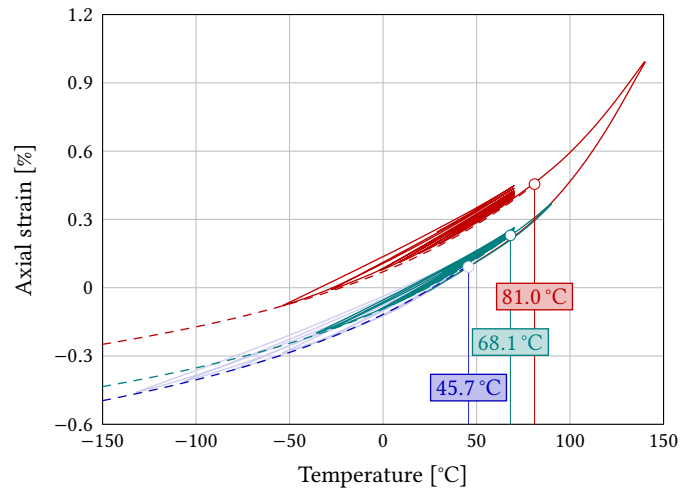
90 °C has been to shift the common origin by about 20 °C, and by about 32 °C for pre-heating at 140 °C. It is interesting to observe that the slopes of re-heating, plotted in Figure 9 against the minimum temperature of the previous cycle, lie on a unique (though scattered) curve, regardless to their previous thermal history. Notice that these slopes are those determined along with

Figure 9   Slopes of the linear parts of heating phases of the experiments illustrated in Figure 8 versus the minimum temperature of the preceding thermal cycle, regardless of the thermal history of each experiment. Dashed curve: Equation (1).
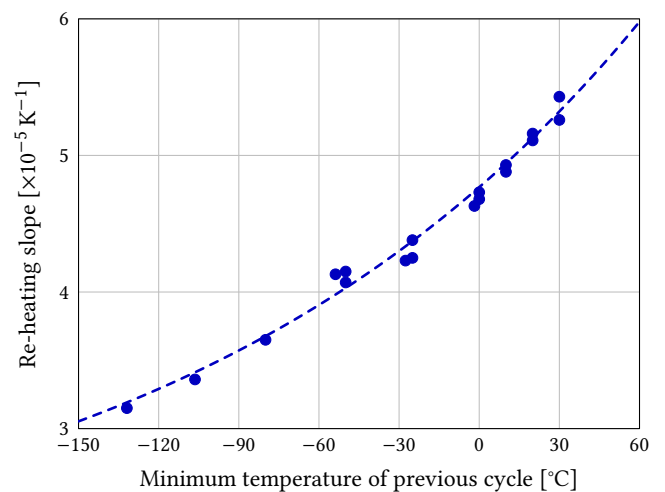
the common origins, and include values higher than the thermal expansion coefficient of the composite in its initial state. This unique curve obeys the equation

$$\alpha(T_{\min}) = \alpha_\infty + \alpha_\triangle \exp\left(\frac{T_{\min}}{T_\triangle}\right) \tag{1}$$

where $\alpha_\infty = 1.77 \times 10^{-5} \, \text{K}^{-1}$, $\alpha_\triangle = 2.98 \times 10^{-5} \, \text{K}^{-1}$, $T_{\min}$ is temperature, expressed in °C, and $T_\triangle = 176.9 \, °\text{C}$.

If, for a particular thermal history, a common origin is chosen, the envelope $\epsilon(T)$ of the cooling curve can be reconstructed using the data of Figure 9 and the expression

$$\epsilon(T) = \epsilon^\star + \alpha(T)(T - T^\star) \tag{2}$$

where $\epsilon^\star$ and $T^\star$ are the coordinates of the chosen common origin, and $\alpha(T)$ is given by Equation (1). Such reconstructions are given as dashed curves in Figure 8. Although purely empirical, this construction may be useful, provided that a means for determining the common origin is available.

3.6 Effect of pre-cooling

Instead of pre-heating and going to low temperature, let now the effect of pre-cooling prior to going at high temperature be examined. Figure 10 compares the case of a cycle at 140 °C, preceded (dark blue) or not (light blue) by a pre-cooling phase at −106 °C. The effect of pre-cooling has

**Figure 10** Hot cycles with (dark blue) and without (light blue) pre-cooling at −106 °C.
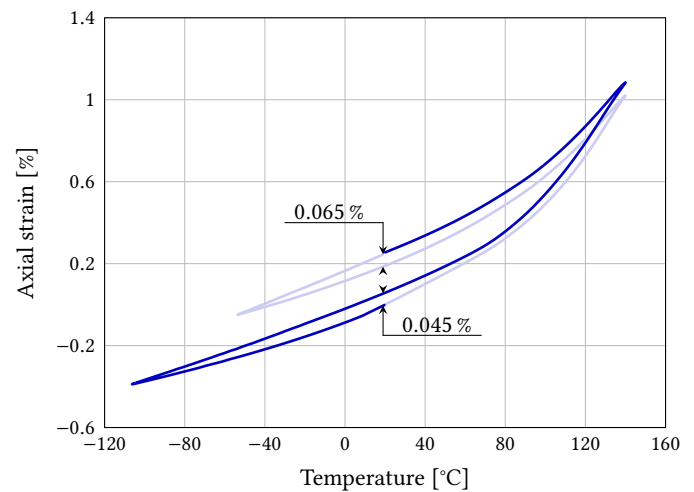
been to increase the residual strain upon cooling back at room temperature, from 0.191 % to 0.256 %, i.e. 0.065 % difference. This is about 40 % higher than the residual strain associated with the pre-cooling phase alone, i.e. 0.045 %. Finally, the fact that both experiments end up at the same residual strain is fortuitous.

It is also observed that the cooling phases from 140 °C are strictly parallel, and this is the case for all cooling phases from 140 °C performed in this work. Encompassing the glass temperature of the binder (~100 °C) seems to erase the past thermal history, apart from residual strains.

3.7 Complex cycles

To conclude this Section, Figure 11 compares double hot cycles at 140 °C separated by cold cycles of different intensities, namely 50 and −50 °C. It shows clearly that the final residual strain

Figure 11 Double hot cycles at 140 °C separated by a cold cycle at 50 °C (blue) and at −50 °C (red). Inset: magnification of the blue curve showing that cooling at 50 °C is not reversible.
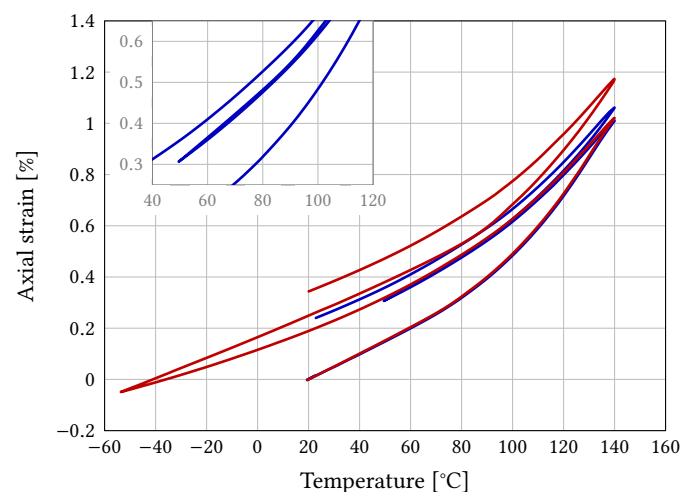
depends strongly on the intensity (i.e. the minimum temperature) of the cold cycle. It also shows (see the inset in Figure 11) that the cold cycle at 50 °C is indeed irreversible.

4 Mesoscale computations

4.1 Motivations

The material at stake displays a quite reproducible thermal expansion response. In its initial state, its approximate reversibility range is [5-75 °C], and its volumetric thermal expansion coefficient, averaged over 16 experiments, is $1.45 \times 10^{-4} \, \mathrm{K}^{-1}$ at ambient temperature, varying by no more than 4 %. This value is 28 % lower than that reported for the TATB single crystal by Sun et al. (2010) and later confirmed by Yeager et al. (2016), i.e. $2.01 \times 10^{-4} \, \mathrm{K}^{-1}$. This is due to the very strong thermoelastic anisotropy of TATB, in the context of randomly oriented crystals, as first suggested by Kolb and Rizzo (1979), and confirmed by Gee et al. (2007), Ambos et al. (2015), and Gasnier et al. (2018b). The experimental value can even be predicted to a quite good accuracy by the formula derived by Hashin (1984) for random hexagonal polycrystals, to which TATB is close. The prediction obtained by adding a thin layer of binder between grains is not significantly modified when the binder is in its glassy domain, and acts as a stress transmitter from grain to grain.

In a purely thermoelastic context, the stress field induced by thermal loading is proportional to temperature, and the conditions for irreversible mechanisms activation are necessarily reached at some temperature level. Such mechanisms are failure of grains and grain-binder interfaces and irreversible deformation of grains and binder. Gee et al. (2007) showed that grain-binder interface failure is likely under heating, while Gasnier et al. (2018b) suggested that grain microcraking be responsible for the decrease of the thermal expansion coefficient of the composite under cooling.

However, none of these authors included the role of irreversible deformation of grains and binder in their investigations. Since local yielding may strongly modify the local stress fields, its role in the local fracture process should be investigated. The purpose of the next Section is to evaluate the influence of local yielding on local stress fields through mesoscale computations. However, since the yield stress of the binder is probably much lower that that of TATB crystals, see Section 4.3 and (Lafourcade et al. 2018; Lafourcade et al. 2019), the following investigation will be limited to the role of binder yielding. Moreover, binder deformation will only be considered in its glassy domain, say below ∼80 °C, in order to put the emphasis on binder (visco)-plasticity and avoid the complexities of viscoelastic behavior when nearing its glass transition.

Therefore, the binder thermomechanical behavior has been characterized, a simple constitutive model identified, and 3D mesoscale computations performed to investigate the role of binder plasticity during thermal cycles. For this purpose, a simple representation of the microstructure and a simplified constitutive model for the binder are considered. More detailed computations including binder viscoplasticity and microcraking are left for future investigations.

4.2 Virtual microstructure

As illustrated in Figure 1, the binder is difficult to visualize, and its morphology in the composite is not well known. However, past studies on the viscoelastic behavior of PBX 9502 (Thompson et al. 2012) under small forced harmonic loading (by Dynamic Mechanical Thermal Analysis) show a strong decrease of the storage (i.e. elastic) modulus when crossing the glass transition, and this is also the case for the present composite (Plassart et al. 2020). This suggests that the binder forms a continuous phase throughout the aggregate. Although it cannot be proven, at the present time, that every grain is entirely coated by the binder (Bennett and Luscher 2019; Bennett et al. 2020), it should be the case for most, and this will be assumed in the sequel.

Our polycrystalline microstructure is based on a Poisson-Voronoi tessellation of space, which, although highly idealized, should be sufficient for the present qualitative investigations. A morphological erosion of the grains by a ball of diameter w yields a continuous binder phase of uniform thickness w. On a regular grid, a thickness of $w \approx 2$ voxels is obtained with a 3D-cross structuring element containing 7 voxels, made of one voxel and its 6 first-neighbours. With an adequate discretization scheme (Gasnier et al. 2018a), such thickness ensures that stress is transmitted from the grains to the binder, not directly from grain to grain. The size of the grains, and so the number of grains on a given domain, is then adjusted to match the binder volume fraction, equal to about 4.5 %. On a 600^3-voxels grid, this is achieved with 400 grains (Figure 12). Note that the domain is the elementary cell of a periodic microstructure. Such property will be
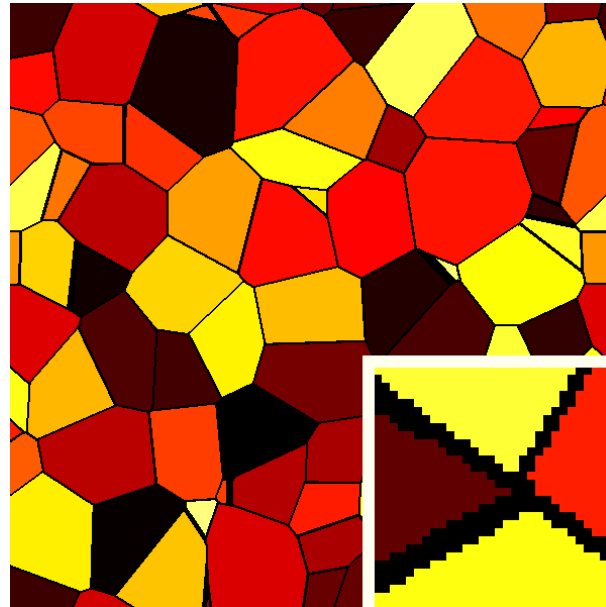
Figure 12   Example of a virtual microstructure (2D slice). Bottom-right: region around a triple-line showing the voxel discretized binder (8 × magnification).

useful later on when applying periodic boundary conditions.

4.3   TATB and binder models

The TATB grains, assumed as homogeneous single crystals, are supposed to be infinitely tough, and TATB plasticity is discarded for the considered loading range (Lafourcade et al. 2018). Their triclinic anisotropic thermoelastic properties are taken from Bedrov et al. (2009) and Sun et al. (2010). Crystallographic orientations are chosen at random, and grain-binder interfaces are supposed infinitely tough.

Figure 13   Binder response to simple uniaxial compression at room temperature.
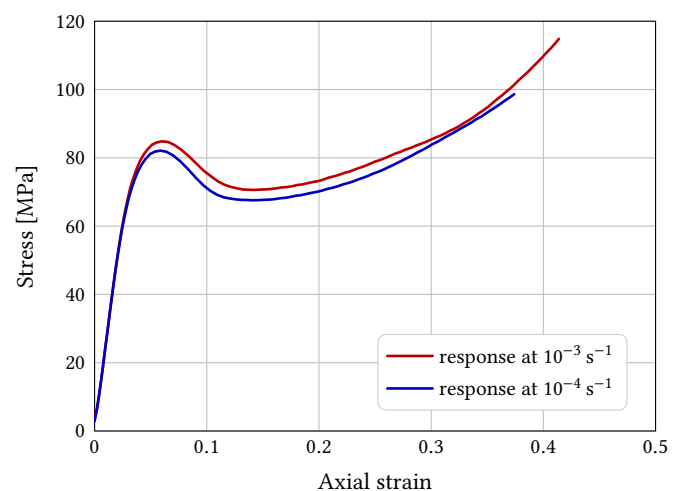
Pure binder specimens were manufactured for uniaxial (stress) tension, shear and compression in the [0-60 °C; 10^{-3}-10^{-5} s^{-1}] range of temperatures and strain rates, and for small strain harmonic oscillations (DMA) in the range [-50-150 °C; 1-300 Hz] range of temperature and frequency. Figure 13 shows examples of compression results at two strain rates and room temperature, and Figure 14 shows an example of DMA result at 1 Hz. In the glassy domain, the results were found to be compatible with the Arruda and Boyce (1993) elasto-viscoplastic model. Briefly, this model describes the dependence of the flow stress, seen as the peak stress of Figure 13, to temperature, strain-rate, stress triaxiality and strain softening and hardening, and neglects nonlinearities observed below the peak stress.

For the present purpose, only the effects of temperature will be considered. The effect of strain-rate will be neglected, assuming that 10^{-5} s^{-1} is representative of the average strain rate

Figure 14 Dynamic Mechanical Analysis at 1 Hz.
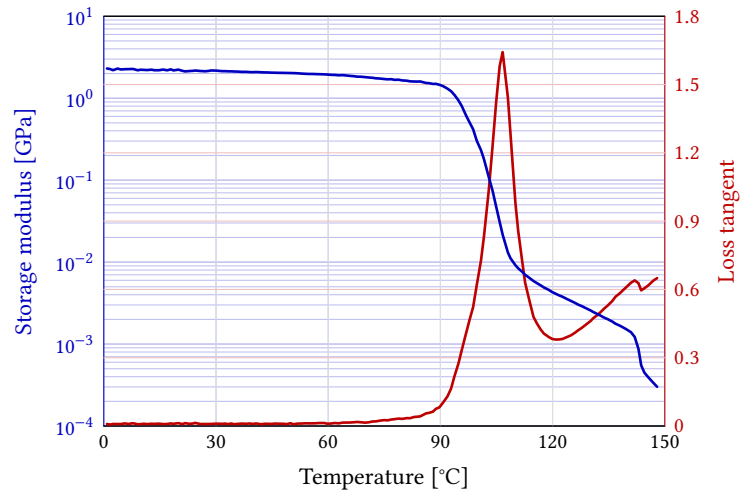
in the binder during thermal loading at $\pm 10\,\mathrm{K\,h^{-1}}$. Therefore, the binder is considered as a temperature-dependent elastic-perfectly plastic material, with elastic (isotropic) properties and flow stress given by

$$K(T) = K_0 + K_0'(T - T_{\mathrm{amb}})$$
$$G(T) = G_0 + G_0'(T - T_{\mathrm{amb}})$$
$$\tau(T, \sigma_m) = S_0(1 + T/(AS_0))^{6/5}$$

(3)

where $\tau = [\frac{1}{2}\boldsymbol{s} : \boldsymbol{s}]^{1/2}$ is the equivalent stress, $\boldsymbol{s} = \boldsymbol{\sigma} - \sigma_m \boldsymbol{1}$ is the deviatoric stress tensor, $\boldsymbol{\sigma}$ is the Cauchy stress tensor, $\sigma_m = \frac{1}{3}\mathrm{tr}\,\boldsymbol{\sigma}$ is the mean stress, $\boldsymbol{1}$ is the identity tensor, S_0 is the athermal flow stress, and K_0, K_0', G_0, G_0', T_{amb}, A and S_0 are material constants given in Table 1. For simplicity, binder thermal expansion is neglected in the sequel.

K_0	K_0'	G_0	G_0'	T_{amb}	A	S_0
GPa	$\mathrm{GPa\,K^{-1}}$	GPa	$\mathrm{GPa\,K^{-1}}$	K	$\mathrm{K\,MPa^{-1}}$	MPa
5.06	-2.22×10^{-3}	0.89	-3.05×10^{-3}	293	-2.586	156.86

Table 1 Material constants used in Equation (3).

4.4 FFT computational framework

Numerical computations in three dimensions are now performed to interpret the role of plasticity in the binder and its effect on the polycrystal, in particular its irreversible deformation during cooling and heating scenarios.

The micromechanical problem involves a set of grains with linear, thermoelastic response embedded in a binder with elastic, perfectly-plastic constitutive law, given by Equation (3). Use is made of a fast Fourier Transform method with Green operator proposed by Willot (2015) for small deformations, which can be directly applied to material images like the one represented in Figure 12, and of the so-called "direct scheme" (Moulinec and Suquet 1994), originally introduced to treat perfectly-plastic phases.

To mimic the experimental setup, the virtual material samples are subjected to zero overall stress, i.e. $\langle \sigma \rangle = 0$, where $\langle \cdot \rangle$ denotes a spatial average, while the microstructure is free to deform ($\langle \varepsilon \rangle \neq 0$) under applied uniform temperature field (i.e. thermal conduction is discarded, owing to the slow heating/cooling rates at stake). Consistently with the representation of the fields in terms of Fourier transforms, periodic boundary conditions are enforced along the boundary of the 3D volume.

Various thermal heating-cooling cycles are applied, starting from an initial temperature $T = T_0$, up to $T = T_{\mathrm{max}}$. The material is then cooled down to its final temperature T_{fin}. At the initial temperature $T = T_0$, the stress and strain fields are uniformly zero. Temperature increments of $\delta T = T^{i+1} - T^i = \pm 1\,°\mathrm{C}$ are employed, except when a value of less than $1\,°\mathrm{C}$ is necessary to reach exactly T_{max} or T_{fin}.

4.5 Numerical results

A first computation is performed from $T_0 = 20\,°C$ to $T = -100\,°C$ and heating back to T_0. Figure 15(a) shows the resulting thermogram (blue), which seems reversible at first sight. The red curve, obtained by subtracting the linear part (with initial slope), shows that plasticity indeed occurs, from $-15\,°C$ upon cooling, and from $-30\,°C$ upon re-heating, leaving a 0.003 % irreversible strain back at ambient temperature. Then, a second computation is performed from $T_0 = 48.7\,°C$ to $T = -100\,°C$ and heating back to T_0. The result is displayed in Figure 15(a) (dotted curves). In this case, plastic yielding begins around $20\,°C$ upon cooling, and around $-30\,°C$ upon re-heating, leaving a 0.006 % dilatancy after heating back to $T_0 = 48.7\,°C$.

In order to estimate the consequences of plasticity on stress fields, Figure 15(b) compares the equivalent plastic strain histograms in the grains and the binder at $-100\,°C$ in the purely elastic case and the elasto-plastic one, for the $T_0 = 48.7\,°C$ case. The differences being small, plasticity can be said to have very little effect upon cooling from the stress-free state, and the corresponding experimental thermograms can be interpreted accordingly.
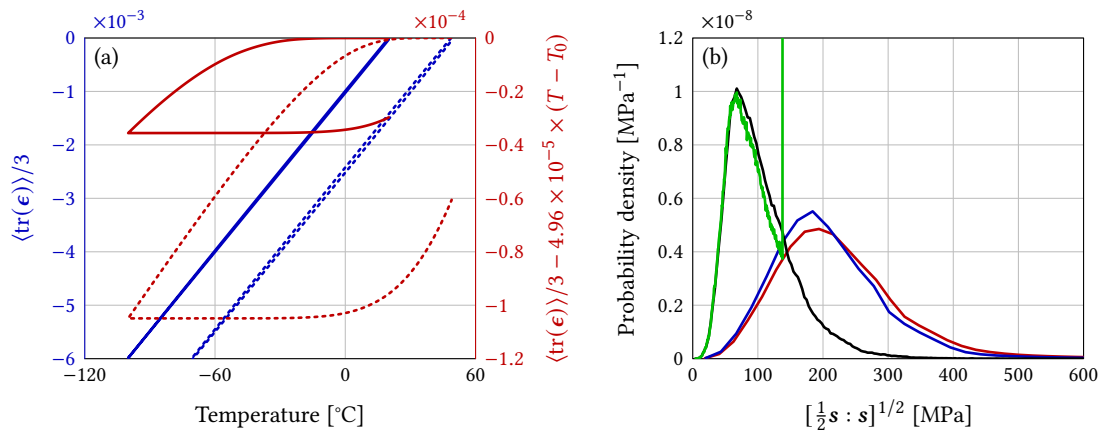

Figure 15   Cooling from T_0 down to $-100\,°C$ and heating back. (a) Thermogram (left vertical axis) and departure from initial linear slope (right vertical axis). Solid: $T_0 = 20\,°C$, dotted: $T_0 = 48.7\,°C$. (b) Case $T_0 = 48.7\,°C$. Histograms of equivalent stress at $-100\,°C$ in the grains (blue and red) and the binder (green and black) for purely elastic cooling (blue and black) and for elasto-plastic cooling (red and green).

The next computations consist in heating from the stress-free initial temperature $T_0 = 20$ or $T_0 = 48.7\,°C$ to $T_{\max} = 80\,°C$, then cooling to $T_{\mathrm{fin}} = -60\,°C$. The resulting thermograms and their nonlinear part are displayed in Figure 16. As was the case for cooling in Figure 15(a), the

Figure 16   Computed thermal cycles from the stress-free state at $T_0 = 20\,°C$ (solid) and $T_0 = 48.7\,°C$ (dotted) to $T_{\max} = 80\,°C$, and cooling to $T_f = -60\,°C$. Left vertical axis: thermograms. Right vertical axis: nonlinear parts.
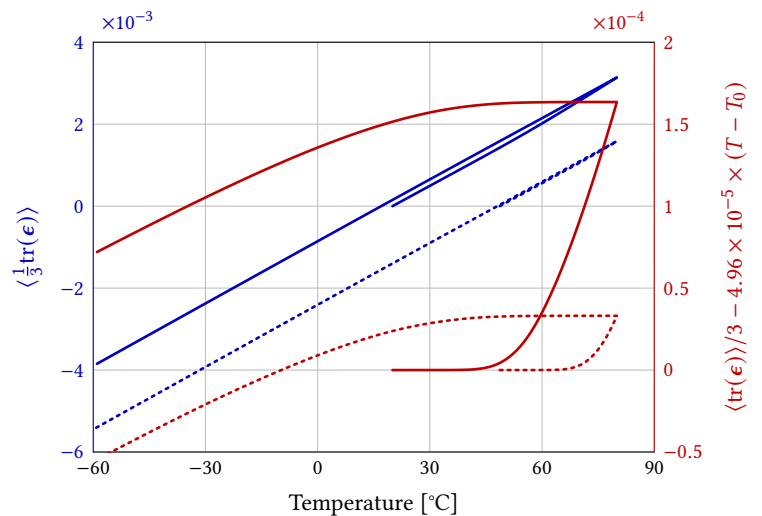
beginning of the heating phase is strictly linear, with a slope of $4.96 \times 10^{-5}\,\mathrm{K}^{-1}$. Linearity is lost at $45\,°C$, the slope increasing slightly up to $80\,°C$. The cooling phase does not coincide with the heating one, and is strictly parabolic. However, its slope varies from 4.93×10^{-5} at $80\,°C$ to $5.07 \times 10^{-5}\,\mathrm{K}^{-1}$ at $-60\,°C$, i.e. only a 3 % increase. The dilatancy at $20\,°C$ is 0.045 %, of the order

of the experimentally measured one (i.e. 0.025 %, see Section 3.3) for the same thermal cycle. For $T_0 = 48.7\,°C$, the dilatancy is only 0.014 % at $T = T_0$.

When $T_0 = 20\,°C$, the irreversible deformation at $T = T_0$ gives rise to heterogeneous strain and stress fields, in both the binder and grains (Figure 17(b)). The volumetric deformation in the binder is both positive and negative, whereas the grains are almost exclusively subjected to negative mean strain, i.e. compression (Figure 17(a)). The mean stresses (Figure 17(b)) remain limited to ±50 MPa approximately, while shear stresses reach much higher values and might influence the microcracking process.
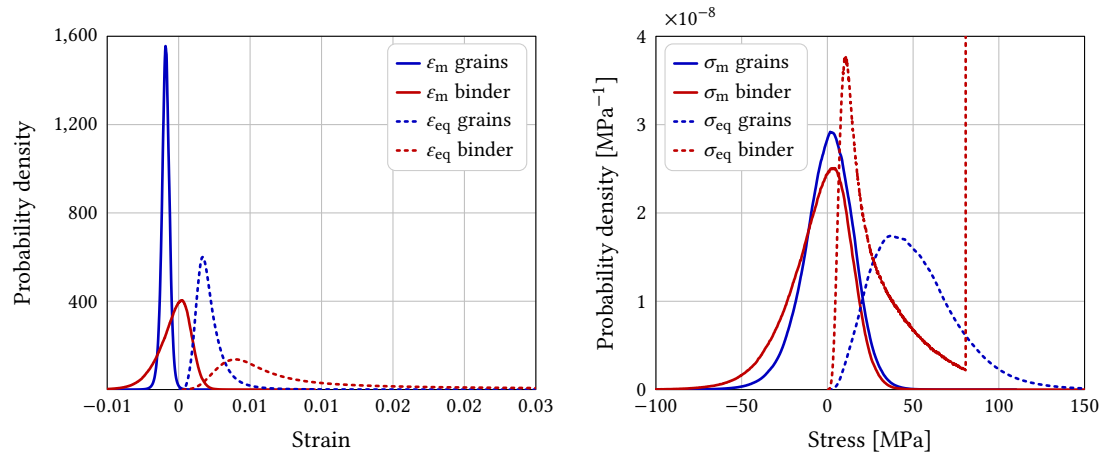

Figure 17   Field histogram for the mean (solid) and von Mises equivalent (dashed) quantities at $T = 20\,°C$, upon heating and cooling, from an initial stress-free state at temperature $T = T_0 = 20\,°C$. (a) Strain, (b) Stress.

Figure 18 shows the evolution of the binder fraction undergoing plastic yielding during a $20 \rightarrow 80 \rightarrow -100\,°C$ thermal cycle, and corresponding FFT field maps for some selected temperatures. The yielding binder fraction increases quite fast upon heating, although the maximum fraction undergoing plastic flow is only 7 %. It decreases more slowly upon cooling, and plastic flow almost stops around $-20\,°C$, prior to increasing again, due to internal stress growth at low temperatures. Note the quasi-symmetry of the curve between 20 and $-70\,°C$, and the corresponding similarity between field maps at those temperatures. In addition, the colored image in Figure 18 gives an idea of residual mean stresses back at $20\,°C$, spanning from -56 MPa (compressive) to 34 MPa (tensile) in grains.

Finally, in order to check the assumption of non viscous plasticity, the histogram for the equivalent plastic shear-rate $\dot{\gamma}_p$ is first computed numerically (Figure 19(a)), obtained for $T_0 = 20\,°C$ and $T_{\max} = 80\,°C$). During heating at $T = 75\,°C$, the plastic strain rate is found to range between 0 and $1.9 \times 10^{-5}\,s^{-1}$ with mean $\overline{\dot{\gamma}_p} = 1.9 \times 10^{-6}\,s^{-1}$. This value is computed over the positive values $\dot{\gamma}_p > 0$ of the plastic strain rate, whereas a peak at 0 is also observed. A narrower distribution is obtained during cooling, with mean $\overline{\dot{\gamma}_p} \approx 4 \times 10^{-6}\,s^{-1}$ at $T = 75\,°C$ and $\overline{\dot{\gamma}_p} \approx 4 \times 10^{-7}\,s^{-1}$ at $T = 0\,°C$. During heating, these values are consistent with our assumptions. During cooling, the mean values are lower than what has been hypothesized, suggesting that the model slightly underestimates the effect of plasticity in the binder.

The assumption of perfect plasticity is also checked in Figure 19(b), which compares the cumulated plastic strain histograms during heating at $80\,°C$ and during cooling at 20 and $-60\,°C$. The maximum plastic strain is ~25 %, remaining outside the range of strong strain hardening (see Figure 13). Figure 19(b) also shows that new plastic zones appear upon cooling, some only slightly plastified, probably corresponding to low temperature yielding (see below and Figure 15).

5   Discussion

The results of Section 4.5 show that upon heating, thermally induced internal stresses are sufficient to induce plastic flow in the binder, more or less precociously depending on the state of internal stresses of the material in its initial state. In the present case, the point is to determine whether residual stresses from the manufacturing process are present or not.
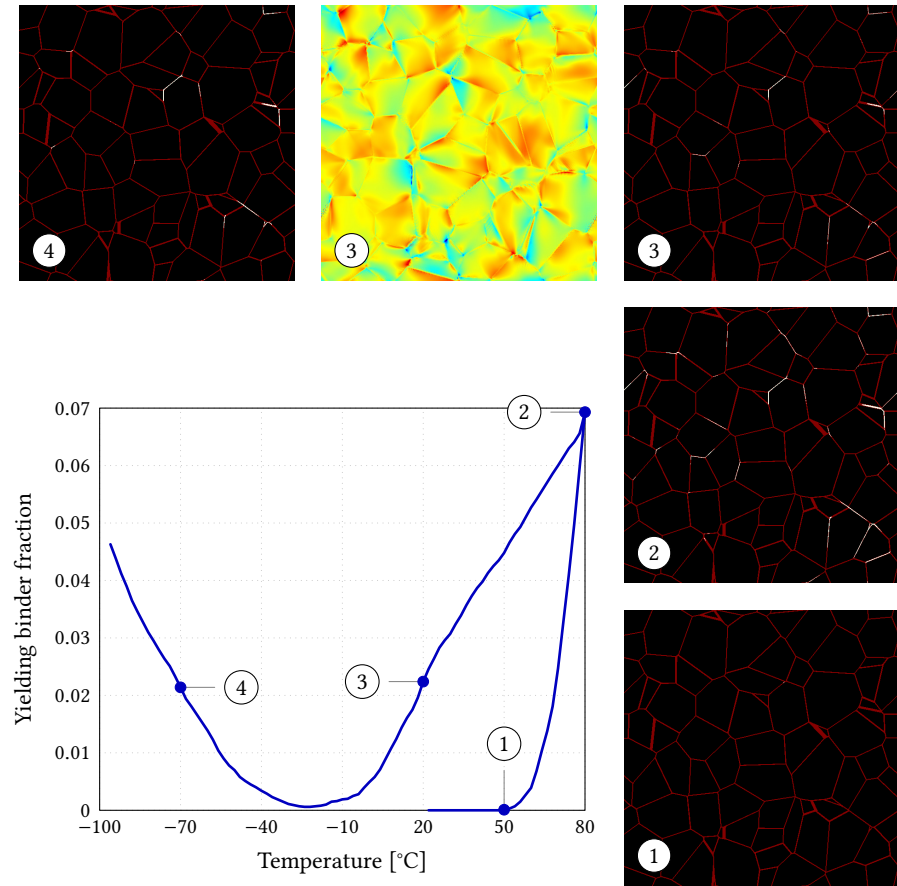
Figure 18   Evolution of the binder fraction experiencing plastic yielding during heating from $T_0 = 20$ to $80\,°C$, and cooling to $-100\,°C$. Each blue dot corresponds to a FFT map of yielding binder (grains in black), from bottom right to top left, during heating at 50 (onset of yielding) and $80\,°C$, and during cooling at 20 and $-70\,°C$. White: yielding. Red: no yielding. The colored image is a map of residual mean stresses back at $20\,°C$. Min: $-56\,MPa$ (blue). Max: $34\,MPa$ (red).

An enlightening example can be drawn from the work of Yeager et al. (2016). Using neutron diffraction, these authors were able to measure the average TATB crystal lattice parameters, either on as-received TATB powder or on a binder-free die-pressed pellet. Their values of the crystal lattice parameters for the loose powder are consistent with those of Cady and Larson (1965) and Sun et al. (2010). In contrast, they found significantly different values for the die-pressed specimen, indicating the presence of strong internal stresses. The latter can be evaluated using the procedure given by Luscher et al. (2014). From the crystal lattice parameters of the loose powder (undeformed state) and the pellet (deformed state), the deformation gradient $F = \frac{\partial x}{\partial X}$ and the strain $\epsilon = \frac{1}{2}(F^\top F - I)$, X and x standing for the coordinates of any material point in the initial and deformed states respectively and I for the identity tensor, are given by

$$F = \begin{bmatrix} 1.0011 & 0 & -0.0298 \\ 0 & 1.0011 & -0.0582 \\ 0 & 0 & 0.9900 \end{bmatrix} \quad \text{and} \quad \epsilon = \begin{bmatrix} 0.0011 & 0 & -0.0015 \\ & 0.0011 & -0.0029 \\ \text{sym.} & & 0.0099 \end{bmatrix}. \tag{4}$$

If this strain is multiplied by the elastic tensor obtained by Bedrov et al. (2009) by a molecular dynamics method, using their "non-polarizable" interatomic force-field, a measure of an average internal stress tensor σ is

$$\sigma = \begin{bmatrix} 52 & 15 & 0 \\ & 25 & -4 \\ \text{sym.} & & -157 \end{bmatrix} \text{MPa} \tag{5}$$

which represents non negligible values, displaying a strong compressive component σ_{33} normal to the graphitic plane of the TATB crystal, as pointed out by Yeager et al. (2016), and in-plane
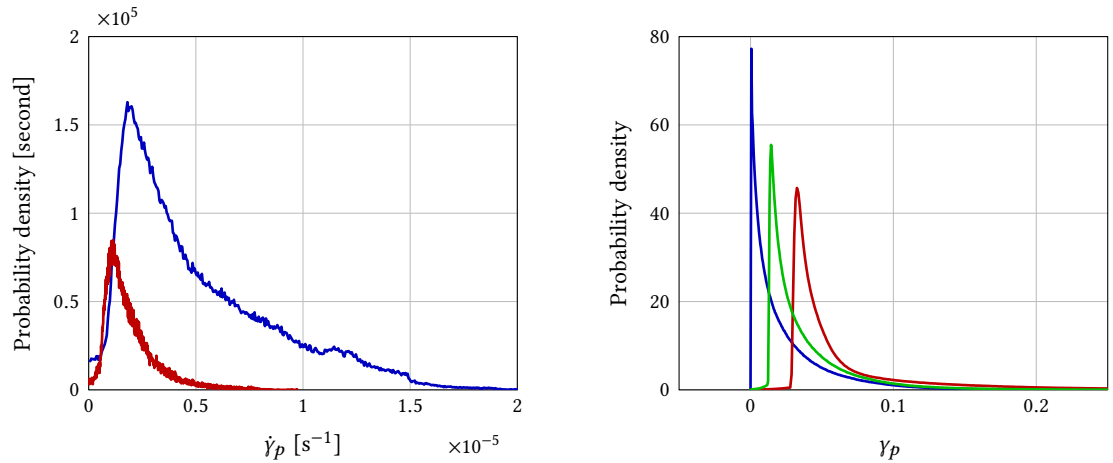
Figure 19 Field histograms. (a) Equivalent plastic strain rate in the binder at 75 °C during heating (blue) and cooling (red) with $T_0 = 20$ °C and $T_{max} = 80$ °C. (b) Cumulated equivalent plastic strain during heating at 80 °C (blue) and during cooling at 20 °C (green) and −60 °C (red).

tensile components σ_{11} and σ_{22}. In this case, such high internal stress levels are induced by plastic yielding of TATB grains during pressing.

The situation is not exactly the same in the composite at stake here, owing to the presence of binder. Pressing being performed in the binder liquid state, cooling first involves crossing the glass transition, bringing the binder in its glassy state. Internal stresses must grow upon cooling, somewhat mitigated by plastic yielding, first strongly due to the low elastic limit at still relatively high temperature, more mildly as temperature decreases. Therefore, internal stresses are very likely to exist at room temperature. However, aging must also take place in the stressed binder, reducing progressively stress levels with time. In the same way, the population of intergranular microcracks suggested by Gasnier et al. (2018b) to exist in the initial state of the composite at stake are very likely to result from cooling after pressing at the end of the manufacturing process.

Bringing the composite from its initial state above the glass transition erases the thermal history of the binder, as is the case for any amorphous thermoplastic polymer. This explains why all experimental cooling curves are identical to a very good accuracy, whatever the previous history of the samples. The consequence is that the material experiences the same cooling as at the end of the manufacturing process, resulting in a new state of residual stresses, with little binder aging, if any, and with new (intergranular) microcracks. Therefore, new residual stresses must be higher than in the initial state.

After such a thermal loading and unloading, a new elastic range is instated. This is evidenced by the difference of cooling curves in Figure 2 and Figure 4. The latter displays totally reversible cycles during cooling and the beginning of re-heating from 50 °C, while the last cooling curve departs from linearity around 50 °C, to be compared to ~5 °C without pre-heating. This is even better seen in the inset of Figure 3 after pre-heating at 90 °C, materialized by an arrow in the inset of Figure 3.

Crossing the glass transition cancels the stiffness of the binder, as shown in Figure 14 and releases most internal stresses, leaving only low level entropic and viscous ones. Individual TATB grains thermal expansion is no more hindered, which explains why the slope of the thermograms (see, for instance, Figure 4) increases so dramatically. Moreover, the strong anisotropy of the thermal expansion implies strain incompatibilities between adjacent crystals of different orientations, thus explaining why this slope is higher than the volumetric thermal expansion coefficient of the TATB crystal.

In this case, stresses being close to zero, it is possible to subtract the volumetric thermal expansion of TATB grains from experimental thermograms. The result, illustrated in Figure 20 for the $100 \rightarrow 140 \rightarrow 100$ °C thermal cycle (light blue), includes porosity and deformation of the binder as well. The behavior of the latter is not well known in this temperature range but should vary between rubbery up to ~120 °C and liquid above (see Figure 14), both highly viscous.

In addition, we have plotted the initial slope (3.18×10^{-4} K^{-1}) of the light blue curve, and

the same slope from the beginning of cooling. Quasi-linearity is observed upon heating up to ~110 °C, and upon cooling down to ~120 °C. This quasi-linear behavior might be attributed to the binder, while the remainder might represent the evolution of porosity, but at this point it would be quite hazardous to go any further without a clear understanding of the binder behavior at high temperature.

Figure 20 Grains thermal expansion subtracted from the thermal expansion of the composite calculated from the data of Figure 2 (red).
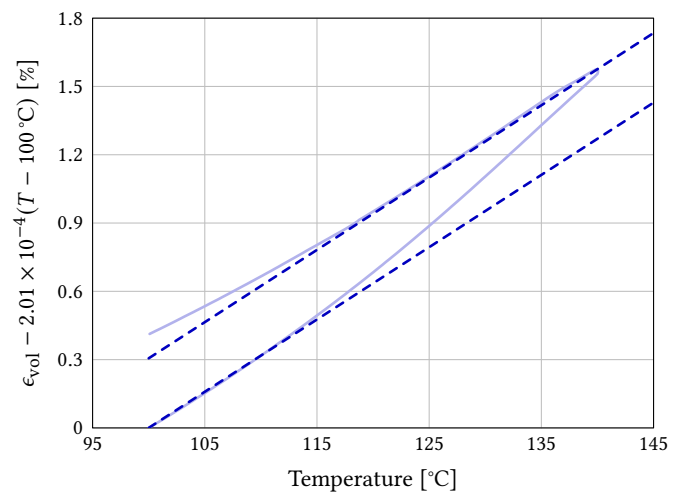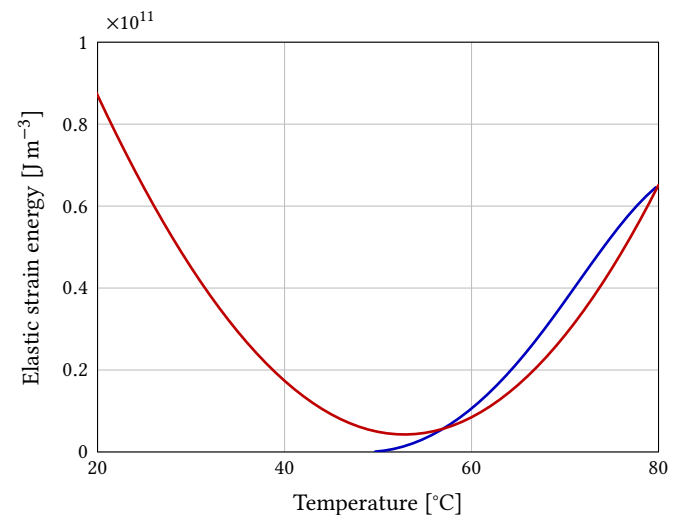

Figure 21 Evolution of elastic strain energy computed for heating from $T_0 = 48.7$ °C to 80 °C (blue) and cooling to -100 °C while preventing binder plastic yielding (red).

Regarding cooling from ambient, the computations having shown that negligible plasticity occurs, the state of residual stresses is not likely to be changed upon coming back to 40 °C, since the microcracking process involves no binder plasticity, although it relaxes internal stresses. This strongly suggests the common origin of Figure 7 to be the temperature at which internal stresses are minimum since, according to the computations, they do not vanish. Although the only way to back this assumption would be to model the entire pressing process, a complementary argument can be provided. Consider the computed thermal cycle of Figure 16. As shown in Figure 21, the elastic strain energy goes through a minimum at ca. 53 °C when performing a virtual elastic cooling by forbidding plastic yielding in the binder. This shows that even a small amount of binder plasticity indeed induces a redistribution of internal stresses, and is capable of shifting the temperature of the (quasi) stress-free state, in the present case by about 4 °C.

This picture does not explain why going to very low temperatures prior to going above the glass temperature and coming back to ambient (Figure 11) increases dilatancy. Up to now, our view of cooling disregarded nonlinear phases at the end of re-heating phases. Such nonlinearities are commonly observed in quasi-brittle materials under alternate tensile-compressive loadings (see for example the experimental work of Nouailletas et al. (2015) on concrete), and are generally attributed to the unilateral effect due to progressive and incomplete microcrack closure upon unloading and reverse loading. In the present case, these nonlinearities are reversible if cooling does not go too far down, and induce some hysteresis otherwise (see the inset of Figure 6). Thus,

incomplete closure of microcracks could perturb internal stresses, and modify the onset of plastic yielding back to higher temperatures, but this clearly needs some additional work to be clarified.

The calculations detailed above should be considered as a first approximation, having been performed with two main simplifying assumptions. The microstructure is highly idealized, in the form of TATB grains and a uniform thickness of binder layers as well. The presence of reduced molecular mobility binder layers in the vicinity of TATB grain surfaces is likely, although the recent work of Parisse et al. (2019) suggests that their thickness might be small with respect to binder layer thickness. Moreover, the temperature dependence of the yield stress was considered as the most prominent feature of the binder behavior, such that thermal expansion and strain rate and pressure dependence of the yield stress have been neglected. Thermal expansion, for instance, could reduce (resp. increase) stress levels upon cooling (resp. heating), delaying (resp. accelerating) plastic yielding, thus having significant effects on the overall response of the composite.

6   Conclusion and future work

The material studied here is characterized by the very high anisotropy of its constitutive crystals, which explains a large part of its unusual thermal behavior. Strong internal stresses occur when thermally loaded, and are likely to be present in the initial state, as the result of the manufacturing process.

The other important mechanisms is plastic yielding of its binder, whose crucial peculiarity is the strong dependence of its yield stress to temperature. The computations, although performed in a simplified context, have shown that this dependence allows easy plastic flow upon heating, inducing some stress release, but plastic flow preclusion upon cooling, thus favouring microcracking processes. They have also allowed to exhibit a state of minimum internal stress levels, dependent on the history of plastic deformation.

The next step will be to perform microstructure-based computations accounting for a more accurate description of binder behavior, as well as for microcracking.

References

Ambos, A., F. Willot, D. Jeulin, and H. Trumel (2015). Numerical modeling of the thermal expansion of an energetic material. *International Journal of Solids and Structures* 60-61:125–139. [DOI], [OA], [HAL].

Armstrong, C. and J. Mang (2021). Thermally-driven changes to porosity in TATB-based high explosives. *Propellants, Explosives, Pyrotechnics* 46:1–10. [DOI].

Arruda, E. and M. Boyce (1993). Evolution of plastic anisotropy in amorphous polymers during finite straining. *International Journal of Plasticity* 9(6):697–720. [DOI].

Bedrov, D., O. Borodin, G. Smith, T. Sewell, D. Dattelbaum, and L. Stevens (2009). A molecular dynamics simulation study of crystalline 1,3,5-triamino-2,4,6-trinitrobenzene as a function of pressure and temperature. *The Journal of Chemical Physics* 131(22):224703. [DOI].

Bennett, K. and D. Luscher (2019). Effective thermoelasticity of polymer-bonded particle composites with imperfect interfaces and thermally expansive interphases. *Journal of Elasticity* 136:55–85. [DOI].

Bennett, K., M. Zecevic, D. Luscher, and R. Lebensohn (2020). A thermo-elastoplastic self-consistent homogenization method for inter-granular plasticity with application to thermal ratcheting of TATB. *Advanced Modeling and Simulation in Engineering Sciences* 7(1). [DOI], [OA].

Cady, H. and A. Larson (1965). The crystal structure of 1,3,5-triamino-2,4,6-trinitrobenzene. *Acta Crystallographica* 18(3):485–496. [DOI].

Drodge, D., D. Williamson, S. Palmer, W. Proud, and R. Govier (2010). The mechanical response of a PBX and binder: combining results across the strain-rate and frequency domains. *Journal of Physics D: Applied Physics* 43(33):335403. [DOI], [HAL].

Ellis, K., C. Leppard, and H. Radesk (2005). Mechanical properties and damage evaluation of a UK PBX. *Journal of Materials Science* 40(23):6241–6248. [DOI].

Gasnier, J.-B., F. Willot, H. Trumel, D. Jeulin, and J. Besson (2018a). Thermoelastic properties of microcracked polycrystals. Part I: Adequacy of Fourier-based methods for cracked elastic

bodies. *International Journal of Solids and Structures* 155:248–256. [DOI], [HAL].

Gasnier, J.-B., F. Willot, H. Trumel, D. Jeulin, and M. Biessy (2018b). Thermoelastic properties of microcracked polycrystals. Part II: The case of jointed polycrystalline TATB. *International Journal of Solids and Structures* 155:257–274. [DOI], [HAL].

Gee, R., A. Maiti, S. Bastea, and L. Fried (2007). Molecular dynamics investigation of adhesion between TATB surfaces and amorphous fluoropolymers. *Macromolecules* 40(9):3422–3428. [DOI], [OA].

Hashin, Z. (1984). Thermal expansion of polycrystalline aggregates: I. Exact analysis. *Journal of the Mechanics and Physics of Solids* 32(2):149–157. [DOI].

Kolb, J. and H. Rizzo (1979). Growth of 1,3,5-triamino-2,4,6-trinitrobenzene. I. Anisotropic thermal expansion. *Propellants, Explosives, Pyrotechnics* 4(1):10–16. [DOI].

Lafourcade, P., C. Denoual, and J.-B. Maillet (2018). Irreversible deformation mechanisms for 1,3,5-triamino-2,4,6-trinitrobenzene single crystal through molecular dynamics simulations. *The Journal of Physical Chemistry C* 122(26):14954–14964. [DOI], [HAL].

Lafourcade, P., C. Denoual, and J.-B. Maillet (2019). Mesoscopic constitutive law with nonlinear elasticity and phase transformation for the twinning-buckling of TATB under dynamic loading. *Physical Review Materials* 3(5):053610. [DOI], [HAL].

Le, V. D., M. Gratton, M. Caliez, A. Frachon, and D. Picart (2010). Experimental mechanical characterization of plastic-bonded explosives. *Journal of Materials Science* 45(21):5802–5813. [DOI].

Luscher, D, M Buechler, and N Miller (2014). Self-consistent modeling of the influence of texture on thermal expansion in polycrystalline TATB. *Modelling and Simulation in Materials Science and Engineering* 22(7):075008. [DOI].

Maienschein, J. and F. Garcia (2002). Thermal expansion of TATB-based explosives from 300 to 566 K. *Thermochimica Acta* 384(1-2):71–83. [DOI].

Moulinec, H. and P. Suquet (1994). A fast numerical method for computing the linear and nonlinear mechanical properties of composites. *Comptes rendus de l'Académie des sciences. Série II. Mécanique, physique, chimie, astronomie* 318:1417–1423. [HAL].

Nouailletas, O., C. La Borderie, C. Perlot, P. Rivard, and G. Ballivy (2015). Experimental study of crack closure on heterogeneous quasi-brittle material. *Journal of Engineering Mechanics* 141(11):04015041. [DOI], [HAL].

Parisse, S., J.-F. Petit, A. Forzy, A. Lecardeur, S. Beaugrand, and P. Palmas (2019). Binder and interphase microstructure in a composite material characterized by scanning electron microscopy and NMR spin diffusion experiments. *Macromolecular Chemistry and Physics* 221(2):1900310. [DOI], [HAL].

Picart, D. and J.-L. Brigolle (2010). Characterization of the viscoelastic behaviour of a plastic-bonded explosive. *Materials Science and Engineering: A* 527(29-30):7826–7831. [DOI], [HAL].

Plassart, G., D. Picart, M. Gratton, A. Frachon, and M. Caliez (2020). Quasistatic mechanical behavior of HMX- and TATB-based plastic-bonded explosives. *Mechanics of Materials* 150:103561. [DOI], [HAL].

Rae, P., S. Palmer, H. Goldrein, J. Field, and A. Lewis (2002). Quasi-static studies of the deformation and failure of PBX 9501. *Proceedings of the Royal Society A. Mathematical, Physical and Engineering Sciences* 458(2025):2227–2242. [DOI].

Rizzo, H., J. Humphrey, and J. Kolb (1981). Growth of 1,3,5-triamino-2,4,6-trinitrobenzene (TATB). II. Control of growth by use of high T$_g$ polymeric binders. *Propellants, Explosives, Pyrotechnics* 6(3):57–62. [DOI].

Schwarz, R., C. Liu, and D. Thompson (2005). *Anisotropy in the ratchet growth of PBX 9502.* Technical Report LA-UR-15-21827. Los Alamos National Laboratory, USA. [DOI].

Schwarz, R., G. Brown, D. Thompson, B. Olinger, J. Furmanski, and H. Cady (2013). The effect of shear strain on texture in pressed plastic bonded explosives. *Propellants, Explosives, Pyrotechnics* 38(5):685–694. [DOI].

Skidmore, C., T. Butler, and C. Sandoval (2003). *The elusive coefficients of thermal expansion in PBX 9502.* Technical Report LA-14003. Los Alamos National Laboratory, USA. [DOI].

Sun, J., B. Kang, C. Xue, Y. Liu, Y. Xia, X. Liu, and W. Zhang (2010). Crystal state of 1,3,5-triamino-2,4,6-trinitrobenzene (TATB) undergoing thermal cycling process. *Journal of Energetic*

Materials 28(3):189–201. [DOI].

Thompson, D., G. Brown, B. Olinger, J. Mang, B. Patterson, R. DeLuca, and S. Hagelberg (2010). The effects of TATB ratchet growth on PBX-9502. *Propellants, Explosives, Pyrotechnics* 35(6):507–513. [DOI].

Thompson, D., R. Deluca, and G. Brown (2012). Time–temperature analysis, tension and compression in PBXs. *Journal of Energetic Materials* 30(4):299–323. [DOI].

Thompson, D., C. Woznick, and R. DeLuca (2019). Thermal cycling and ratchet growth of TATB and PBX 9502. *Propellants, Explosives, Pyrotechnics* 44(7):850–857. [DOI], [OA].

Trumel, H., P. Lambert, G. Vivier, and Y. Sadou (2010). Toward physically-based explosive modelling: meso-scale investigations. *Materials under Extreme Loadings: Application to Penetration and Impact.* Ed. by E. Buzaud, I. R. Ionescu, and G. Z. Voyiadjis. J. Wiley & sons. Chap. 9, pp 179–204. [DOI], [HAL].

Wiegand, D., B. Redingius, K. Ellis, and C. Leppard (2011). Pressure and friction dependent mechanical strength – cracks and plastic flow. *International Journal of Solids and Structures* 48(11-12):1617–1629. [DOI], [OA].

Willey, T., T. van Buuren, J. Lee, G. Overturf, J. Kinney, J. Handly, B. Weeks, and J. Havsky (2006). Changes in pore size distribution upon thermal cycling of TATB-based explosives measured by ultra-small angle X-ray scattering. *Propellants, Explosives, Pyrotechnics* 31(6):466–471. [DOI].

Willey, T., M. Hoffman, T. van Buuren, L. Lauderbach, R. Gee, A. Maiti, G. Overturf, L. Fried, and J. Ilavsky (2009). The microstructure of TATB-based explosive formulations during temperature cycling using ultra-small-angle X-ray scattering. *Propellants, Explosives, Pyrotechnics* 34(5):406–414. [DOI].

Williamson, D., S. Palmer, W. Proud, and R. Govier (2007). Brazilian disc testing of a UK PBX above and below the glass transition temperature. *AIP Conference Proceedings* 955:803. [DOI].

Willot, F. (2015). Fourier-based schemes for computing the mechanical response of composites with accurate local fields. *Comptes Rendus Mécanique* 343(3):232–245. [DOI], [OA], [HAL].

Woznick, C., D. Thompson, R. DeLuca, B. Patterson, and T. Shear (2018). Thermal cycling and ratchet growth of as-pressed TATB pellets. *AIP Conference Proceedings* 1979:060011. [DOI].

Xu, F., N. Aravas, and P. Sofronis (2008). Constitutive modeling of solid propellant materials with evolving microstructural damage. *Journal of the Mechanics and Physics of Solids* 56(5):2050–2073. [DOI].

Yeager, J., D. Luscher, S. Vogel, B. Clausen, and D. Brown (2016). Neutron diffraction measurements and micromechanical modelling of temperature-dependent variations in TATB lattice parameters. *Propellants, Explosives, Pyrotechnics* 41(3):514–525. [DOI], [OA].

Authors' contributions   H.T. and F.W. conceived the presented ideas. M.B. and T.P. carried out the experiments. H.T. performed the post-treatment. F.W. and F.R. performed the numerical computations. H.T. and F.W. wrote the initial draft and all the authors discussed the results and proposed corrections.

Supplementary Material   None.

Ethics approval and consent to participate   Not applicable.

Consent for publication   Not applicable.

Competing interests   The authors declare that they have no competing interests.

Journal's Note   JTCAM remains neutral with regard to the content of the publication and institutional affiliations.